

Cover Page



Universiteit Leiden



The handle <http://hdl.handle.net/1887/138674> holds various files of this Leiden University dissertation.

Author: Vlieg, R.C.

Title: Two-photon multifocal microscopy for in vivo single-molecule and single-particle imaging

Issue Date: 2020-12-14

Chapter 3

Two-photon multifocal microscopy for *in vivo* single particle tracking

Microscopic tracking of single particles by fluorescence microscopy is a powerful technique to study life processes at the molecular scale. Whereas single-particle, and even single-molecule, tracking in individual cultured cells has been used widely and yielded spectacular results, nanometric imaging and tracking in larger multicellular samples remains challenging, due to the increased scattering of light, increased out-of-focus fluorescence and reduced resolution in the third dimension. Using two-photon – rather than one photon – excitation relieves these constraints but requires a higher excitation power, which is commonly achieved using confocal microscopy. However, such a serial acquisition scheme severely limits the frame rate and generally can not resolve the fast dynamics of nanometric particles. Moreover, the high power that is required to obtain sufficient contrast severely reduces the photostability of commonly used fluorescent labels. Here we explore the possibilities of scanning two-photon multifocal microscopy for *in vivo* single particle tracking. We show that the combination of a modern scientific CMOS camera, which features a higher sensitivity and very low dark signal, with a reduced power per focus and a reduced duty cycle for excitation yields extraordinary low bleaching rates, framerate larger than 10 Hz and a field of view of 100's of microns while maintaining the advantages of two photon excitation. We demonstrate the use of this novel microscopy modality in zebra fish embryos and rapeseed pollen, and show that it allows for multicolor imaging, using spectral selection in either excitation or emission. Furthermore, we show that single gold nanorods in the veins of zebra fish embryos can be tracked with nanometric accuracy, resolving temporal fluctuations in bloodstream velocity. The unprecedented photostability in combination with the reduced background suggests that it should be possible to resolve single fluorescent proteins *in vivo* with two-photon multifocal microscopy.

Vlieg, R. C., Siemons, C., Arias-Alpizar, G., Papadopoulou, P., Boutilier, K., van Noort, J., Two-photon multifocal microscopy for *in vivo* single particle tracking. *In preparation*.

3.1 INTRODUCTION

Single particle tracking (SPT) can uniquely reveal molecular dynamics in cells¹. The brightness and longevity of the used chromophore is an important metric for a SPT measurement. Cellular proteins can be fluorescently labeled via genetic incorporation for highly specific tagging with minimal steric hinder². Inside larger organisms however, scattering and absorption of the weak signal obstructs the detection of single fluorophores. Also, once a fluorophore is bleached the tagged structure can no longer be detected. Markers such as quantum dots³, gold nanorods⁴ (GNRs) or liposomes⁵ tackle the limited signal and photostability of fluorescent proteins while bio-functionalization allows for specific labeling⁶. A protein can be tracked for much longer as signal originates from a multitude of fluorophores or luminescence. In larger organisms however, out-of-focus fluorescence and scattering lowers signal-to-noise ratio (SNR) which impedes detection and tracking of particles. Spinning-disc microscopy is able to detect particles at larger depths by rejecting photons outside the focal plane. Still, excitation of out-of-focus fluorophores is wasteful and the sample is more prone to photobleaching or phototoxicity.

Two-photon microscopy (TPM) tackles out-of-focus fluorescence by confining excitation to the focus of the objective^{7,8}. With signal solely originating from the focus, depletion of out-of-focus fluorophores is eliminated while background is greatly reduced without the need for a pin-hole aperture. Moreover, the near-infrared excitation wavelength is less prone to absorption and scattering in tissue compared to visible wavelengths⁹. This further reduces photo-toxicity, autofluorescence and increases the depth at which particles can be detected¹⁰. These advantages make TPM a promising technique for deep and long time-lapse imaging. However, single-beam scanning and the relative weak two-photon absorption cross section of fluorophores impedes imaging acquisition times – making TPM unsuitable for SPT¹¹.

Two-photon multifocal microscopy (TPMM) improves acquisition speeds by multiplexing the excitation beam. Distributing a high laser power (2-3 Watt) over multiple beamlets increases scanned volume proportional to the number of foci. Multiplexing of the excitation beam can be achieved via passive components such as: beam-splitters^{12,13}, micro-mirrors¹⁴, diffractive optical elements^{4,15} (DOEs) and spatial light modulators¹⁶⁻²⁰ (SLMs). Kilohertz acquisition speeds are possible by under-sampling of the field-of-view (FOV) via random-access scanning using SLMs²⁰⁻²³. These high frame rates have been used for fast imaging of calcium waves in brain cells. However, the reliance on structural information from a prior scanned image makes it unsuited for capturing the unpredictable behavior of single particles. Recently, SPT was realized by two-photon tomography, which illuminates a sample using lines instead of traditional excitation points. Scanning lines of excitation across the focal plane at multiple angles allows

to rapidly reconstruct the full FOV via back-projection algorithms. Although relatively complex, this method was able to track fluorescent beads *in vitro* in a volume of 250 μm diameter and 250 μm depth at 10 Hz²⁴. Another approach is target-locking a single particle based on its estimated position from the ratio of four tetrahedral positioned foci²⁵. Via spatiotemporal splitting of the laser beam, temporal resolutions down to 50 μs inside opaque spheroids have been realized. Although achieving impressive depth and (temporal) resolution, the method is limited to tracking a single particle per measurement. Arguably, most straightforward technique for SPT is to rapidly sample a full FOV by scanning a fixed beamlet-pattern. The excitation beam is split by a single element, while fast scanning (galvanometric) mirrors sample the focal plane. Signal from the multiple foci are captured via camera detectors for inherent wide-field detection. Via this method, nanometric wide-field tracking of single GNRs inside cells has been achieved by spiral scanning a 10 x 10 array of beamlets⁴.

The abovementioned designs focus on maximizing framerates for highest temporal resolution and requires relative high excitation powers. However, while signal increases quadratic to laser power, bleaching increases with a power larger than 2^{26,27}. Therefore, longer time-lapse measurements would favor minimum excitation power and consequently low count-rate per fluorophore. To compensate for a low-count rate, without impeding acquisition speeds, a larger number of foci is favorable to minimize the area a single beamlet has to sample.

Here we investigate the merits of TPMM with a relative large number of foci for high acquisition speeds combined with low photo-damage. We adopt the straightforward approach of spiral-scanning an array of 25 x 25 beamlets using a high-efficient DOE to create a homogeneous virtual-light sheet. The accessible design retains a single high-NA objective for high resolution and easy mounting of samples. Rapid refresh rates allow to gently optically dissect samples while single particles in zebrafish embryos (*Danio rerio*) and rapeseed embryos (*Brassica napus*) can be readily observed. The combination of low photobleaching, high framerates and low background make TPMM a very compelling imaging technique and our findings here show promise that it could even be used for single molecule tracking studies.

3.2 MATERIALS AND METHODS

Microscopy setup. A tunable near-IR Ti:Sa laser (Coherent, Chameleon Ultra) was coupled into a home-build two-photon multifocal microscope. A diffractive optical element (DOE, custom made by Holo-eye) diffracted the laser beam into an array of 25x25 foci. A fast-scanning mirror (Newport, FSM-300-1) driven by an Archimedean spiral rapidly scanned the beams yielding a fairly homogeneous wide-field illumination, as characterized before⁴. The laser beams were focused using a 25X NA 1.1 water dipping objective (Nikon, CFI75

Apochromat 25XC), illuminating an area of 180 μm x 180 μm . Except when stated otherwise, a single period of the spiral scan took 100 ms and was synchronized with the camera. TPL was collected by the same objective, filtered with a dichroic mirror (Semrock, 700dcxr) and two short pass filters (Semrock, FF01-720-SP & FF01-750-SP) and focused on a 2048 x 2028 pixel back-illuminated sCMOS camera (Photometrics, Prime BSI). Additional band pass filters, mounted in a motorized fast-change filter wheel (Thorlabs, FW103H/M), could be positioned in front of the camera. The excitation wavelength, scanning mirror, stepper motor and camera were controlled by self-written LabVIEW (National Instruments) software.

Gold nanorod sample. GNRs with a central plasmon resonance of 808 nm (Nanopartz, A12-10-808) were embedded in a plastisol environment and sandwiched between two glass coverslips according to previously established protocol²⁸. This yielded a transparent sample with a random distribution of GNRs in three dimensions. Excitation wavelength was set at 800 nm to efficiently excite GNRs at their plasmon resonance. Diffraction limited spots were sorted based on maximum intensity and a 3D Gaussian (eq. 3.1) was fitted onto a volume of 11 x 11 x 21 pixels per spot.

$$I(x, y, z) = A \exp\left(-\left(\frac{(x - x_0)^2}{2w_x^2} + \frac{(y - y_0)^2}{2w_y^2} + \frac{(z - z_0)^2}{2w_z^2}\right)\right) + C \quad (3.1)$$

With the amplitude A , offset C , x_0 y_0 and z_0 are the centroids of the Gaussian in x , y and z coordinates. The width of the Gaussian is defined by w_x , w_y and w_z . The sub-pixel coordinates (x_0, y_0, z_0) were used to align the measured spots onto a 6 times interpolated grid, yielding a smoothed average PSF in both longitudinal and axial plane, as shown in Figure 3.1b.

The theoretical localization uncertainty σ between consecutive z -stacks was calculated using the model of Thompson et al²⁹:

$$\sigma = \sqrt{\frac{s^2}{N_p} + \frac{a^2}{12N_p} + \frac{8\pi s^2 b^2}{a^2 N_p^2}} \quad (3.2)$$

where s is the width of the PSF, N_p the number of detected photons, a the pixel size and b the number of background photons. Note that eq. 3.2 does not account for three-dimensional data. Previous research has shown that the model matches experimental results within 1 nm error³⁰.

Zebrafish embryos. Zebrafish (*Danio rerio*, strain AB/TL) were maintained and handled according to the guidelines from the Zebrafish Model Organism Database (<http://zfin.org>) and in compliance with the directives of the local animal welfare committee of Leiden University. Fertilization was performed by natural spawning at the beginning of the light period, and eggs were raised at 28.5 °C in egg water (60 $\mu\text{g}/\text{mL}$ Instant Ocean sea salts). Previously established

*Tg(kdrl:mCherry)*³¹, *Tg(kdrl:eGFP)*³² and *Tg(kdrl:mTurquoise)*³³ zebrafish lines were used to label the vascular system. Rhodamine B labeled liposomes consisting of DSPC + LU3 were synthesized in-house by the SBC group of the Leiden Institute of Chemistry. A detailed description on the transfection and culturing of carcinoma cells can be found in previous published work⁵. In short, PC-3 M-Pro4 cells were labeled with mCherry and transfected with miR-221-5p 48 hours before inoculation.

The liposomes or gold nanorods [10 nM] were injected into 84 or 56 hours post fertilization (hpf) zebrafish embryos using a modified microangiography protocol. Before injection, embryos were anesthetized in 0.01% tricaine and embedded in 0.4% agarose containing tricaine. To improve reproducibility of microangiography experiments, 1 nL volumes were calibrated and injected into the sinus venous/duct of Cuvier. After the injection needle penetrated the skin, it was gently pulled back, thereby creating a small pyramidal space in which the liposomes and gold nanorods were injected. Successfully injected embryos showed backward translocation of venous erythrocytes and absence of damage to the yolk ball. Using the same method, around 400 PC-3 M-Pro4 carcinoma cells were injected and imaged one-day post injection.

Zebrafish embryos were mounted onto the sample holder of the microscope. If micro-injections were unnecessary, zebrafish were embedded directly into the agarose-tricaine mixture and mounted onto the microscope sample holder.

Rapeseed pollen. The LEC1:LEC1-eGFP reporter line was generated according to previous established methods^{34,35}. In short, a 3110 base pair (bp) DNA fragment starting 1292 bp upstream of the transcription start site was amplified by PCR and recombined into pGKGWG using the Gateway cloning system (Invitrogen). This construct was consequently transformed to a *Agrobacterium tumefaciens* strain C58C1 carrying the PMP90 Ti plasmid and then to *B. napus*.

Microspores from *Brassica napus* cv DH12075 were isolated according to a previously established protocol for *B. napus*³⁶. Flower buds for culture were selected on length (2.6 to 4.0 mm) and their microspores were isolated and cultured in NLN-13 medium. To induce embryogenesis, microspores were cultured in the dark at 33 °C for 20 hours, and afterwards at 25 °C. Non-induced microspore cultures were cultured at 25 °C. Once isolated, microspores were inoculated in medium containing trichostatin-a (TSA) in DMSO (Sigma-Aldrich), or solely DMSO for the control microspores, and cultured for another 20 hours at 33 °C or 25 °C. Afterwards, cultures were centrifuged at 200g for 3 minutes and re-suspended in fresh NLN-13 medium absent or TSA at 25 °C.

The SNR of regions of interests (ROIs) in the pollen images was defined as:

$$\text{SNR} = \frac{I_{\text{signal}} - I_{\text{background}}}{\mu_{\text{background}}} \quad (3.3)$$

where I_{signal} is the average signal intensity, $I_{background}$ the average background intensity, and $\mu_{background}$ the standard deviation of the background intensity.

Bleaching. The signal intensity I as a function of time for the bleaching measurements in zebrafish and pollen embryos was fitted to:

$$I = A e^{-t/\tau} + C \quad (3.4)$$

with amplitude A , offset C , time t and decay time τ .

Theoretical count rate. We estimated the TPE intensity from a single fluorophore based on the probability of TPE per pulse (p)⁷:

$$p \approx \frac{p_0^2 \delta}{\tau_p f_p^2} \left(\frac{(NA)^2}{2hc\lambda} \right)^2 \quad (3.5)$$

where p_0 is the average laser intensity per focus, δ the two-photon absorption cross section of the fluorophore at wavelength λ , τ_p the duration of a single pulse, f_p is the repetition rate of the laser, NA the numerical aperture of the objective, h is Planck's constant, and c is the speed of light.

From eq. 3.5 we find the expected count rate (I_{signal}) by taking the collection efficiency of the setup (η) into account, the duty cycle (DC) of a single spiral scan, and the quantum efficiency of the fluorophore (Q).

$$I_{signal} = p * f_p * \eta * DC * Q \quad (3.6)$$

η was estimated on the collection efficiency of the objective (0.20, NA=1.1), the multiple filters and optical elements in the emission path and the quantum efficiency of the camera (0.93). This results in $\eta = 0.10$. The DC was estimated as the spot size divided over the field-of-view it has to scan. At 25X magnification, the distance between two neighboring foci is 9.0 μm (data not shown) and the size of a pixel is 0.26 μm . Further, based on the results in Figure 3.1c, the PSF width is 0.4 μm . From these values we estimate a DC of 0.00425

3.3 RESULTS

3.3.1 OPTICAL SECTIONING

To characterize the resolution of the microscope and the thickness of the virtual light-sheet we measured the 3D point spread function (PSF) using gold nanorods (GNRs) embedded in a

plastisol environment. GNRs form diffraction limited, bright, non-blinking and non-bleaching point sources. 164 GNRs were detected in a volume of $180 \mu\text{m} \times 180 \mu\text{m} \times 100 \mu\text{m}$, sampled in slices of $0.3 \mu\text{m}$. The maximum intensity projection shown in Figure 3.1a shows randomly distributed GNRs as distinct spots with varying brightness. This variation in brightness is expected from the narrow TPE spectrum in combination with a somewhat poly-disperse GNR population, resulting in off-resonance excitation for some GNRs. Moreover, aggregation of rods causes some spots to appear excessively bright and non-diffraction limited. All individual spots were fitted to a 3D Gaussian (equation 3.1).

To ensure that only single GNRs were included, spots with a lateral FWHM ($\text{FWHM}_{x,y}$) $> 0.75 \mu\text{m}$ axial height (FWHM_z) $> 3.0 \mu\text{m}$ were excluded. Fits with a R-squared < 0.1 were also excluded from further processing. Using the filtered x, y and z offsets, 124 regions of interest (ROIs) were aligned and summed, yielding an averaged 3D image representing the PSF, shown in Figure 3.1b. The profiles of the average PSFs (black line) partially follow the theoretical lateral and axial minimum resolution for TPE (solid red line) of $0.400 \mu\text{m}$ and $0.863 \mu\text{m}$ ⁸. In addition, the profiles have a weaker secondary component which fits to a Gaussian with $\text{FWHM}_{x,y} = 0.75 \mu\text{m}$ and $\text{FWHM}_z = 2.19 \mu\text{m}$. These values are higher than the theoretical $\text{FWHM}_{xy} = 0.46 \mu\text{m}$ and $\text{FWHM}_z = 1.37 \mu\text{m}$ for a one-photon PSF, as would be expected for scattering by the GNR. This suggests that besides linear contrast mechanisms, averaging the 124 GNRs has broadened the peaks further. Additional emission filters will reduce scattered photons which should narrow especially the axial PSF. Still, the narrow two-photon PSF will be dominant for labels that have a smaller scattering cross-section than GNRs, and shows how TPE confines excitation compared to linear contrast mechanisms.

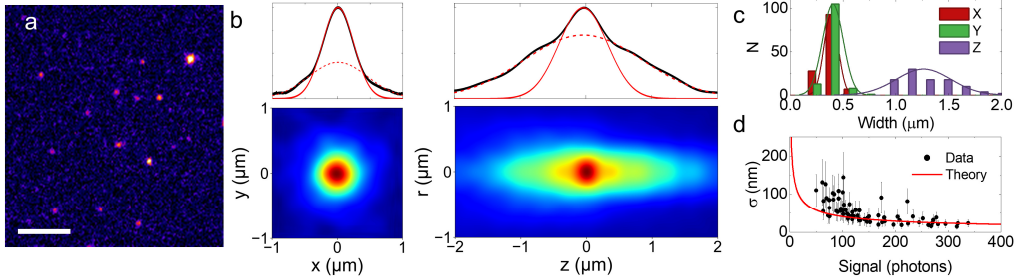


Figure 3.1: Multifocal scanning in combination with two-photon excitation allows for high resolution wide-field imaging. (a) Max intensity projection of a volume of gold nanorods imbedded in plastisol. Scale bar = $10 \mu\text{m}$. (b) Average point-spread function in lateral and axial plane of 124 GNRs. Profiles (solid black line) are overlaid with two Gaussians. One Gaussian (solid red line) corresponds to expected theoretical profile and the second Gaussian (dashed red line) is fitted to the broader component of the profile. The theoretical Gaussians have a $\text{FWHM}_{xy} = 0.4 \mu\text{m}$ and $\text{FWHM}_z = 0.86 \mu\text{m}$. The fitted curve yields $\text{FWHM}_{xy} = 0.86 \mu\text{m}$ and $\text{FWHM}_z = 2.2 \mu\text{m}$. (c) The distribution of both the lateral and axial PSF from fitting a Gaussian to all detected GNRs. The average resolution in the lateral plane is $0.39 \pm 0.08 \mu\text{m}$ with an axial resolution of $1.26 \pm 0.26 \mu\text{m}$. (d) Localization precision is shot-noise limited.

The distributions of the FWHM of individual GNRs in x , y and z are plotted in Figure 3.1c and nicely match the expected diffraction limit of $0.4 \mu\text{m}$, with $\text{FWHM}_x = 0.39 \pm 0.07 \mu\text{m}$ (mean \pm SD) and $\text{FWHM}_y = 0.40 \pm 0.09 \mu\text{m}$, but show a small eccentricity due to optical aberrations in the emission path. $\sigma_z = 1.3 \pm 0.3 \mu\text{m}$ is significantly larger than the expected value of $0.86 \mu\text{m}$. The larger mean FWHM_z likely originates from scattering and one-photon excitation, as previously addressed. The larger width in z is also seen in Figure 3.1b where the amplitude of the secondary components is approximately twice as large as in x, y .

Besides resolution enhancement due to the non-linear absorption, accurately localizing point sources can further improve image resolution. We quantified the reproducibility of localizing single spots by repeatedly imaging a volume of $180 \mu\text{m} \times 180 \mu\text{m} \times 40 \mu\text{m}$ of the fixed GNR sample. The average 3D localization differences between consecutive measurements are shown in Figure 3.1c. Experimental values follow the theoretical limit (equation 3.2) which indicates that localization precision is shot-noise limited. Localization errors due to shot noise can be reduced with increased luminescence intensity by using a high excitation power. We refrained from doing so as a higher power greatly reduces GNR stability due to melting³⁷. Nevertheless, GNRs were localized in 3D with shot-noise limited super resolution accuracy.

3.3.2 PHOTBLEACHING

Fluorescent proteins and organic dyes also feature limited stability upon optical excitation. TPM is associated with high excitation powers and consequently high in-focus photobleaching rates which may reduce biological damage and may limit the duration of fluorescence microscopy. We investigated the photobleaching rates of three different fluorescent proteins expressed in live three-day post fertilization (*dpf*) zebrafish embryos. The embryo expressed either: eGFP, mCherry or mTurquoise in endothelial cells by the fusion of fluorescent proteins to the vascular endothelial growth factor *kdrl*. After immobilization in agarose gel, images of brain blood vessels were taken continuously with an average excitation power of 1.44 mW per focus. A previously recorded wide-field transmission image, shown in Figure 3.2a, shows the orientation of the head, with the large eyes as reference structures. It also shows the large extend of light scattering, despite the transparency of the fish. The wide-field TPL images retain sharp features despite this scattering, indicating that the optical sectioning of TPE is sufficient to reject most scattering, which is achieved in confocal imaging by the pinhole.

First, we imaged blood vessels in eGFP-expressing embryos, shown in Figure 3.2b. Thin blood vessel walls are interspersed with larger spots that mark the location of nuclei of the endothelial cells. After 30 minutes of continuous imaging at 4 fps we see negligible decrease in fluorescence. Despite fixation in agarose, movement of the embryo during the measurement shifted the blood vessel $20 \mu\text{m}$ to the right. In the z -direction the blood vessel remained within the excitation plane, implying that entry of new eGFP from out-of-focus regions by a drift of the excitation plane cannot explain the absence of bleaching. In contrast to eGFP, continuous

excitation of mCherry, as shown in Figure 3.2c, resulted in much faster bleaching of fluorescence. mTurquoise, displayed in Figure 3.2d, showed similar absence of bleaching as with eGFP.

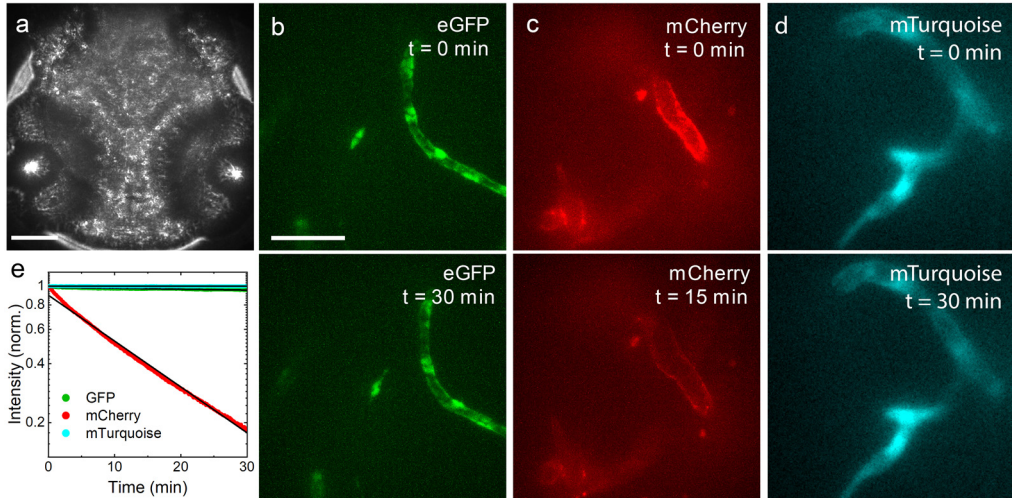


Figure 3.2: Photobleaching is reduced by averaging the excitation power over multiple foci. (a) Transmission image of the head of a zebrafish embryo. (b) eGFP stained endothelial cells of blood vessels inside a zebra fish embryo brain. Scale bar = 50 μm . (c) mCherry stained endothelial cells are almost completely depleted from fluorescence after 30 minutes of imaging. (d) mTurquoise shows similar limited bleaching as eGFP. (e) Signal intensity over time fitted to eq. 3.3, yielding $\tau = 16.1 \pm 0.3$ hours for eGFP, $\tau = 310 \pm 25$ hours for mTurquoise and $\tau = 17.4 \pm 0.1$ minutes for mCherry. Scale bar = 25 μm .

To quantify the bleaching rate, we integrated the signal of a 25 μm x 25 μm ROI and plotted the intensity in time (Figure 3.2e). The intensity was fitted to an exponential decay function to extract the decay time of the fluorescence. Under continuous illumination, eGFP shows a decay time of $9.7 \pm 0.2 \times 10^2$ minutes and mTurquoise $18.6 \pm 1.5 \times 10^2$ minutes. The bleach rate of mCherry is significantly shorter with 17.4 ± 0.1 minutes. The initial deviation from the exponential decay may in this case be explained by small axial drift of the sample or by single-photon bleaching. Overall, eGFP and mTurquoise, with their negligible bleaching, are better suited for long-term time-lapse imaging than mCherry. Nevertheless, all fluorophores show sufficient stability to acquire >1000 frames.

3.3.3 BACKGROUND SUPPRESSION

A major advantage of TPE for *in vivo* imaging is background suppression via reduced autofluorescence and reduced scattering due to near-infrared excitation. To illustrate this, and to test whether this advantage remains for multifocal wide-field microscopy, we imaged *Brassica napus* (rapeseed) pollen embryos and compared the results with one-photon confocal

3.3 Results

microscopy. Specific fluorescence labeling was introduced by expression of the transcription factor LEFY COTYLEDON1 (LEC1) fused with eGFP. LEC1 plays a key role in regulating seed development and is expressed from the moment a single pollen grain enters embryonic state³⁸. As a transcription factor, LEC1 is expected to reside inside the nucleus. Interestingly however, it was reported to be present anywhere inside the cytoplasm, suggesting poor targeting to the nucleus after transcription³⁹. We also observed this in one-photon confocal images of two-day and three-day old pollen embryos, shown in Figure 3.3a and 3.3b. eGFP signal is distributed throughout the embryos with highest signal in the nucleus. The nucleolus is distinguishable as a low intensity area residing within the nucleus (white arrows, Figure 3.3a). The left-most pollen grain in Figure 3.3b has just entered embryonic state and only traces of LEC1:eGFP are expressed. In the cytoplasm, low concentration of LEC1:eGFP contrasts with the pollen wall that is visible via autofluorescence. Overall, confocal microscopy suggests that LEC1:eGFP is relatively homogeneously distributed within the pollen embryos.

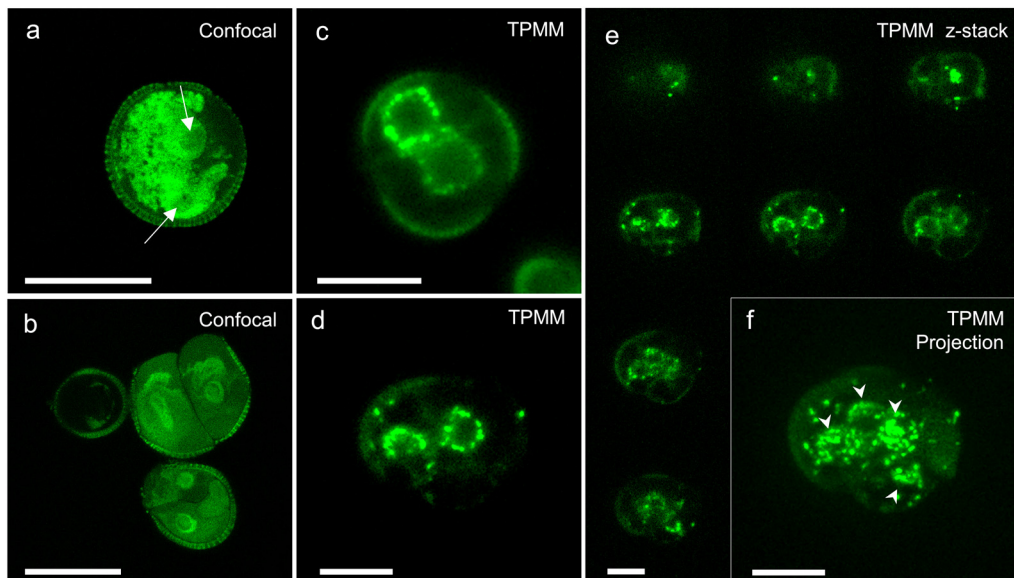


Figure 3.3: TPMM reveals localized LEC1:GFP expression at high contrast inside pollen embryos. (a) A two-day old pollen embryo imaged using one-photon confocal microscopy. LEC1:GFP shows to be homogeneously distributed throughout the pollen embryo. (b) Confocal image of four-day old pollen grains. The more developed embryo has undergone more divisions, with LEC1:GFP distribution imaged similarly as in *a*. (c) A TPMM image of a similar pollen embryo as in *a*. Where in confocal LEC1:GFP was captured dispersed throughout the embryo, here it is imaged as highly localized puncta oriented around the nucleus. (d) TPMM image of a four-day old pollen embryo, similar to *b*. Again LEC1:GFP is concentrated around the nucleus as distinct puncta. (e) Z-stack of the same pollen grain as in *d* showing an image every 2.4 μm apart. LEC1:GFP is located throughout the pollen grain, with highest concentration around the nuclei. (f) Maximum intensity projection the z-stack in *e*. Here the location of the nuclei can be clearly seen as they are surrounded by LEC:GFP puncta. Scale bars = 25 μm .

Imaging similar pollen grains with TPE reveals a different picture, as shown in Figure 3.3c. LEC1:eGFP signal is predominantly located around the nuclei in distinct puncta, in contrast to the homogeneous distribution we saw with confocal microscopy. In non-induced pollen, no accumulation of fluorescence was observed, see Figure S3.1. The pollen wall was visible in both strains, though significantly reduced in intensity as compared to LEC1:eGFP. There is the large difference in acquisition time between confocal (56 seconds) and TPMM (0.1 seconds). Similar noise levels (μ) were achieved by averaging 20 TPMM images (2 seconds), see Figure 3.2S. The SNR of the cytoplasm is similar in confocal images and the TPMM. In the TPMM measurement of the non-induced pollen, SNR in the cytoplasm was at the same level, indicating that this signal should not be attributed to eGFP. The bright puncta in TPMM have a 3.5-fold increase in SNR compared to the eGFP signal in the confocal images. The average signal of 5 LEC1:eGFP puncta was measured to be 684 ± 64 photons. Considering acquisition time of 0.1 seconds and a duty cycle of 1 ms per pixel, we estimate an average count rate of $6.8 \times 10^5 \pm 6.3 \times 10^4$ photons/sec per punctum. With an average excitation power per focus of 1.4 mW, we expect a count rate of 8.6×10^3 photons/sec for a single eGFP molecule (eq. 3.5). These calculations suggest that the puncta consist of about 80 LEC1:eGFP proteins. In the TPMM image of a three-day old pollen embryo, shown in Figure 3.3d, most LEC1:eGFP is again clustered in the nucleus, though LEC1:eGFP puncta also appear near the pollen wall. The intensity per punctum increased to $1.30 \pm 0.03 \times 10^6$ photons/sec, indicating strong accumulation of hundreds LEC1 proteins per spot. So it appears that LEC1 aggregates at the periphery of the nucleus during development. From these results, confocal imaging revealed that LEC1:eGFP is homogeneously distributed in the cytoplasm. Surprisingly however, it did not capture the bright puncta observed in TPMM. TPMM did yield LEC1:eGFP in the cytoplasm.

The entire pollen grain was imaged in 150 z-slices of $0.3 \mu\text{m}$ to study LEC1:eGFP distribution in three dimensions, as shown in Figure 3.3d. A selection of the slices is displayed in Figure 3.3e. Three nuclei in the pollen grain at different heights can be clearly distinguished from the accumulation of LEC1:eGFP near the nuclear membrane. The three-dimensional image shows that LEC1:eGFP appears to be isotopically distributed over each of the nuclei. Though a small number of individual puncta appear to be scattered near the pollen wall as well. From the maximum intensity projection, shown in Figure 3.3f, we count about 20 out of 120 spots that are not located near the nuclei (white arrowheads). In summary, the thin virtual light sheet created by TPE allowed to optically dissect a pollen grain in 3D, and resolved individual puncta of LEC1:eGFP that were scattered in the nuclei. Differences in contrast between confocal and TPMM were apparent for the imaging of pollen embryos. Finally, the reduced acquisition time potentially increases the throughput and allows for rapid time lapse imaging.

3.3.4 SINGLE PARTICLE TRACKING

To test the potential for time-lapse imaging we evaluated SPT in live zebrafish embryos. GNRs were intravenously microinjected in three day old embryos, where they circulated freely in the bloodstream. Embryos were sedated with tricaine (50 $\mu\text{g}/\text{mL}$) and embedded in agarose gel for stability and imaged directly after the gel hardened. A blood vessel located in the brain, as depicted in Figure 3.4a, was continuously imaged at 10 frames per second (fps). GFP-expressing endothelial cells mark the blood vessel wall and show a T-junction just below the skin of the embryo. Tissue surrounding the blood vessel also features luminescence, which may be due to second harmonic generation (SHG) from collagen in the skin⁴⁰. This signal was more dominant in the upper-head area. Note the slightly patterned features in the image that originate from imperfect scanning parameters. The deeper lying blood vessels featured less background. However, the concentration of GNRs was too high to accurately distinguish single GNRs.

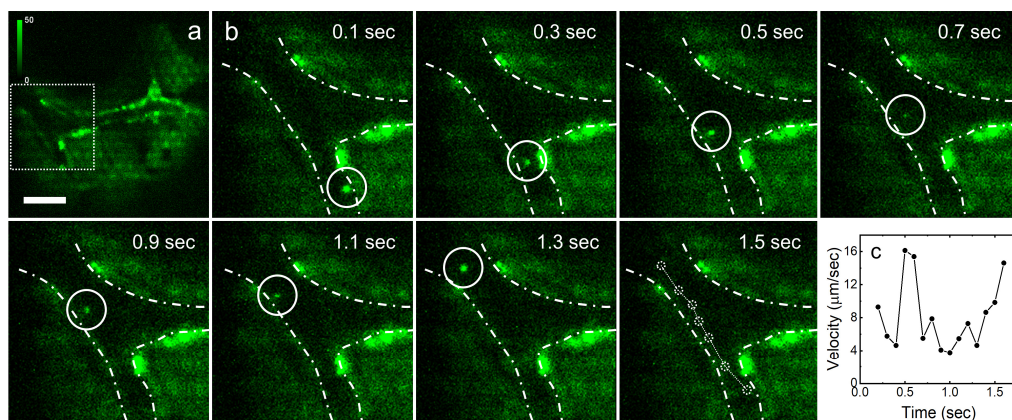


Figure 3.4: Sub-second tracking of a single gold nanorods in zebrafish embryos. (a) Image of a blood vessel surrounded by endothelial cells in the brain of an embryo. Scale bar = 25 μm . (b) Close-ups of the blood vessel (white square, a). A GNR appears on the bottom (white circle) and is captured at 10 fps as it moves along the vessel. (c) Graph with the trend in velocity of the GNR between every taken image. Speed goes up around 0.5 seconds, while also increasing 1 second later at 1.5 seconds.

During acquisition, multiple GNRs were passing through the vein, as shown in Figure 3.4b (white square). To guide the eye, the blood vessels are annotated by white dotted lines and the location of the GNR by a white circle. After the GNR enters the ROI, it travels along the direction of the blood stream. It takes approximately 1.5 seconds for the GNR to cover a distance of 22.5 μm before disappearing outside the FOV. During the time 15 images were taken and the location of the GNR in each image was extracted. The signal intensity varied somewhat due to the GNR moving in and out of focus. Nevertheless, the GNR could be tracked continuously and its velocity is plotted in Figure 3.4c. The velocity varied between 4 and 16 $\mu\text{m}/\text{sec}$ in a 1 second

interval. This oscillation in speed corresponds with heart rates found in embryos sedated by similar dosage of tricaine⁴¹. Tracking single particles in live zebrafish embryos nicely demonstrates the ability of TPMM to visualize dynamics of nanometric structures *in vivo*.

3.3.5 MULTI-COLOR IMAGING

Like one-photon fluorescence, TPE has two ways of achieving multicolor imaging: the differences in both excitation and emission spectra can be exploited to separate orthogonal fluorophores. As TPE spectra are not commonly found in literature, we first measured the excitation spectra of three fluorescent proteins and an organic dye in our microscope. In doing so, we also characterized the spectral response of all elements in the excitation and emission path. Over a range between 730 nm and 1000 nm the laser power gradually increased and reached a maximum power of approximately 900 mW at 800 nm, plotted in Figure 3.5a, corresponding to 1.44 mW per focus. The spectrum follows laser specifications, except for a small periodic modulation, resulting in dips at 780, 845 and 875 nm. These dips are likely caused by interference of the filters in the excitation path. Due to the quadratic dependence of TPE on excitation intensity, the small dip in the excitation spectra at 785 nm would result in a $\pm 30\%$ fluorescent signal reduction. The dip at 815 nm would result in 11% reduced signal. Moreover, the global variation in laser power over the entire spectrum, would modulate signal by a factor of 18. Though the power spectrum of the laser could be used to correct the fluorescence emission, we refrained from doing so as we cannot exclude that part the detected signal originates from either scattering or OPE, making such corrections highly non-trivial.

Having measured the laser spectrum, we next measured the excitation spectra of rhodamine B, mCherry, mTurquoise and eGFP expressed in endothelial cells in zebrafish embryo brains. Excitation spectra were acquired by continuous imaging, while sweeping the excitation wavelength between 730 nm and 1000 nm, using a 700 nm low-pass emission filter. Signal intensities were measured by integrating over an area of $50 \mu\text{m} \times 50 \mu\text{m}$ and the resulting normalized spectra are shown in Figure 3.5b. mTurquoise, GFP and rhodamine B all featured a maximum signal at 830 nm. As expected the modulation in excitation power spectrum is more pronounced in the TPE spectrum. mCherry has maximum excitation at 750 nm, which rapidly drops at wavelengths larger than 810 nm. This difference in excitation spectrum allows for simultaneous imaging with the other fluorophores by alternating the excitation wavelength. The difference in excitation between rhodamine B and eGFP can also be used for multi-color imaging when switching between 830 and 870 nm. Rhodamine B features a distinctive peak at 880 nm that can be exploited despite the three times lower laser power at this wavelength. However, mCherry has the most distinguishable spectrum, allowing two-color imaging with any of the other dyes.

3.3 Results

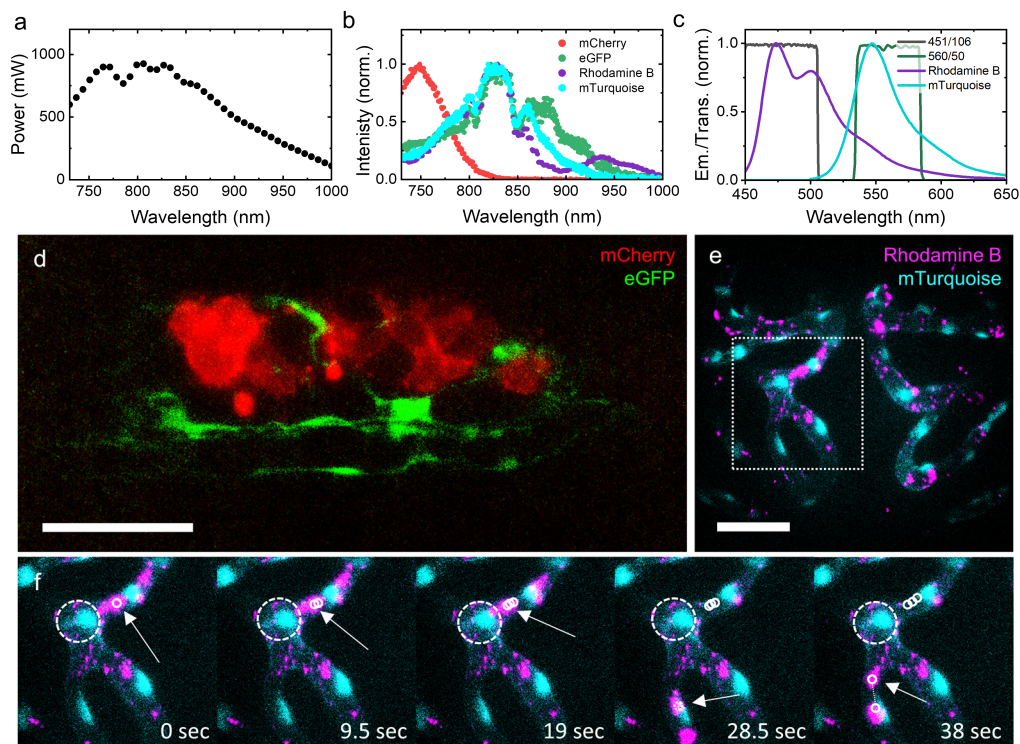


Figure 3.5: Multi-color imaging by alternating either excitation wavelength or the emission filter. (a) Power spectrum of the laser measured at the sample stage. The power unexpectedly dips at 770 nm and 820 nm due to interferences in the excitation path. (b) Excitation spectra of four commonly used dyes. (c) Tailored band pass filters to spectrally separate fluorophores. (d) Carcinoma (mCherry, red), located in the tail of a zebra fish embryo, is resolved from surrounding endothelial cells (eGFP, green) by changing the excitation wavelength of the laser. (e) Liposomes (rhodamine B, magenta) line the endothelial cells (mTurquoise, cyan) inside a zebra fish embryo brain. (f) Liposome aggregates, likely endocytosed by macrophages, are imaged from 5e, inset as they travel through the blood vessels. Scale bars = 50 μm .

To demonstrate this, we imaged human carcinoma cells injected into a 2dpf zebrafish embryo. Carcinoma cells were stained with mCherry while the endothelial cells the embryo expressed eGPF. Two images were measured at 750 nm and 830 nm and displayed in separate colors in Figure 3.5d. Again thin blood vessel walls (green) featured thicker regions that reveal the location the nuclei of the endothelial cells. Larger areas of green signal are attributed to more complex networks of endothelial cells. The mCherry channel exposes individual carcinoma cells (red) lying around the framework of blood vessels. Carcinoma cells on the left appear brighter compared to the ones on the right, which may be explained by maturity of the cells, or variations in mCherry expression. These images were recorded with an integration time of 100 ms. Overall, switching between wavelengths is a viable method for multi-color TPE imaging and can be used to study the dynamic progression of cancer metastasis in live embryos.

Though changing the excitation wavelength can be achieved with 40 nm/sec, the more common approach is to change the emission filters, which may yield faster and/or better contrast multi-color images. The shared excitation peak of rhodamine B and mTurquoise at 830 nm, in combination with a large difference in the emission spectrum, plotted in Figure 3.5c, was used to test this mode. Liposomes loaded with rhodamine B that were intravenously injected into 3dpf embryos with mTurquoise expressing endothelial cells. Two emission filters separate the emission of rhodamine B (maximum at 475 nm) and the emission of mTurquoise (maximum at 560 nm), and were alternated to capture separate channels. Due to spectral leakage we expect 25% of signal in the 451/106 channel to originate from rhodamine B, instead of mTurquoise.

The liposomes are expected to be distributed throughout the embryo, like the GNRs, while also adhering to the blood vessel walls. Each liposome was loaded with approximately 1000-3000 rhodamine B molecules. After injection, a volume of $150\ \mu\text{m} \times 150\ \mu\text{m} \times 30\ \mu\text{m}$ of the brain was imaged in 9.5 seconds while automatically alternating the emission filters. The overlay of two maximum intensity projections for each channel is shown in Figure 3.5e, with mTurquoise in cyan and rhodamine B in magenta. The network of blood vessels is easily distinguished from the dark background in the mTurquoise channel. Similar to Figure 3.5d, the endothelial nuclei featured bright patches on the walls of the veins. The thin blood vessel walls appeared to be decorated with liposomes, visible as diffraction limited spots. We expect that each spot originates from a single liposome. Larger spots are tentatively attributed to aggregated liposomes.

Besides immobile spots, freely circulating liposomes were also visible. Figure 3.5f shows an example of aggregates of liposomes moving through a blood vessel. Each image is the maximum intensity projection of the two channels at the location annotated in Figure 3.5e (white dotted square). The speed at which the aggregates move suggests that the liposomes have been endocytosed by macrophage cells. The first aggregate travels along the blood vessel where it disappears after 19 seconds. It may have left the imaged volume through a blood vessel, moving upwards, indicated by the white dotted circle. The second annotated aggregate, which appears at 28.5 seconds, most likely travels via the same blood vessel out of view after 38 seconds. By overlaying the two channels, the liposome distribution could be positioned to well-defined boundaries of the blood vessels, demonstrating the use of TPMM microscopy to capture dynamic events in live zebrafish embryos with diffraction limited resolution.

3.4 DISCUSSION AND CONCLUSION

Due to its confocal set-up, TPM is generally slow, hampering rapid time-lapse imaging. Here, we characterized the abilities of TPMM for video-rate imaging of biological tissues. Confinement of excitation together with the rapid scanning of multiple foci resulted in a virtual light sheet with a thickness of 1.2 μm . The virtual light sheet allowed us to optically dissect pollen embryos in 3D and accurately resolve LEC1:eGFP distribution inside. While maintaining high resolution and low background, we could also track single GNRs and liposomes inside the brain blood vessels of zebrafish embryos. Using TPMM, we observed that common protein and organic dyes in endothelial cells of zebrafish embryos showed remarkably long fluorescent decay times of up to 310 hours. By either changing the excitation wavelength or by alternating between emission filters, different structures inside zebrafish embryos were readily imaging in 3D using multi-color imaging.

The reduced duty cycle in TPMM, combined with an improved, low-noise sCMOS camera allowed for a low excitation power of typically 1.4 mW per focus while maintaining SNR > 10. Gentle illumination resulted in a photobleaching time of 16 ± 0.3 hours for eGFP. The bleaching rate of eGFP as a function of laser power has been measured to increase with a power of 2.69⁴². This sensitive relation between excitation power and bleaching explains the low bleaching we observe at 1.4 mW per focus. The two-photon fluorescent stability as a function of power has not been characterized for mTurquoise and mCherry. Interestingly however, for OPE, mTurquoise showed to be the most sensitive for bleaching with a power of 1.89, compared to 1.23 for eGFP⁴³. Although the bleaching mechanism by OPE and TPE have been described to be different^{26,44}, the higher sensitivity of mTurquoise with OPE to laser power corresponds to the reduced bleaching decay of $3.1 \pm 0.1 \times 10^2$ hours in TPMM. mCherry bleached several orders of magnitude faster, despite having similar OPE bleaching characteristics to eGFP⁴⁵. However, exciting mCherry at 750 nm may bring it in a higher energetic state than at its primary two-photon absorption peak at 1080 nm^{11,46}. Previous research indicate that faster photobleaching processes can occur at these higher energetic states by formation of ion pairs^{44,47}. The high fluorophore stability that we report here for the other fluorescent proteins suggests that photo-damage can be reduced by exciting the fluorophore to its lowest excited energy state.

In addition to fluorophore stability, non-fluorescent absorption causes damage in biological systems. Imaging with low photo-toxicity is therefore essential for any *in vivo* environment. Pollen embryos studies using OPE for example, have been limited to short timespans and selectively on embryos late in culture, as photodamage at earlier stages prevented long experiments⁵⁰. Based on the extremely low bleaching rate, TPMM may extend imaging

times to allow visualization from initial embryogenesis to more developed stages, while achieving similar resolution and reduction of out-of-focus scattering.

Previous TPMM studies focused on imaging speed or image depth with higher excitation power per focus. Common TPMM designs use linear patterns of up to $64^{13,50}$ foci, or arrays of $8 \times 8^{51,52}$ or $10 \times 10^{18,20}$ foci. At ± 10 times more excitation power available per focus and more rapid scanning an order of magnitude faster imaging rates at similar FOV could be realized. However, the required higher power comes at a cost of increased bleach rate. On the other hand, decreasing power inevitably results in lower brightness, which subsequently requires longer integration time. For longer time-lapse microscopy experiments, it may therefore be favorable to maximize the number of beamlets rather than scanning a limited number of high power beamlets at a faster pace. Parallel imaging using multiple beamlets can be implemented in several ways. Although constrained in design pattern, a DOE-based TPMM provides a simple, high efficient method for increasing temporal resolution. Alternatively, SLM would be a more flexible choice to tailor the illumination pattern according to a specific sample. However, the necessary adaptation of phase-maps complicates design and associated artefacts should be tackled for proper illumination¹⁸. Therefore, introduction of a DOE may be better suited for practical applications in laboratories that do not want to invest in advanced optics.

A different strategy for improving contrast without increasing the excitation power, is to use brighter labels. GNRs exhibit an absorption coefficient that is two orders of magnitude larger than that of organic dyes⁵³. This efficient excitation, mediated by their localized surface plasmon resonance, proved sufficient to resolve single GNRs as labels inside zebra fish embryos. Previous TPM studies using GNRs were limited to single cells^{4,54-57}, or could only resolve clusters of GNRs inside larger model organisms where scattering is prominent when imaging deeper into the tissue^{58,59}. This exemplifies how TPMM can overcome these effects of scattering in deep tissue, without compromising on resolution or FOV. GNRs can be functionalized in a straight-forward manner to target specific proteins inside live animals^{60,61}. Tracking such functionalized GNRs with nanometer accuracy in 3D will give a better insight into physiological pathways of nanoparticles, and may reveal new mechanisms of delivery that could enhance targeted delivery of nano-medicines. Alternatively, we imaged single liposomes inside zebrafish embryos. Liposomes can be loaded with large quantities of fluorophores⁶² and have previously been used in zebrafish embryos as model systems for targeted drug carriers^{5,63}. Here we achieved a frame rate of 10 Hz in 2D and 1 Hz in 3D, allowing for detailed time-lapse analysis. The low bleaching conditions enabled imaging of single liposomes for extended periods of time, showcasing the use of TPMM for following single particles *in vivo*.

Similarly, TPMM was able to resolve LEC1:eGFP inside vesicles located around the nucleus of pollen embryos. Interestingly, confocal OPE microscopy, revealed more homogeneously distributed LEC1:eGFP in the embryo. A previous confocal study also showed a homogenous distribution of LEC1 in both the nucleus and cytoplasm, similar to our confocal observation⁶⁴. In *Arabidopsis* embryos however, LEC1 aggregation inside the nucleus was also

observed by confocal microscopy, resembling our TPMM images of rapeseed pollen³⁹. The difference in contrast that we observe may be explained by several factors. First, autofluorescence of other structures than LEC1:eGFP may contribute to the signal in the confocal microscope, whereas TPM may be less affected. This may be strengthened by the better optical sectioning that is achieved by TPE. Of course it could also be that the difference originated from biological variance. To test this, the same pollen should be imaged in both modalities. TPE would be advantageous for imaging more developed pollen which are bigger and will thus benefit more from the reduced scattering. Suppression of background signal in plant tissue via TPE has been shown in recent studies⁶⁵⁻⁶⁸. TPMM adds to these findings by the increased temporal resolution.

Multi-color imaging in TPM is well established. Here we combine it with the rapid image acquisition of multifocal scanning. Having a tunable laser, it was possible to alternate mCherry and eGFP with a lag-time of ± 5 seconds. Alternatively, emission filters can be switched to separate mTurquoise and rhodamine B using the same excitation wavelength. Tri-color TPM however, has been found challenging due to overlapping emission spectra or inefficient TPE absorption and required more complex excitation strategies such as spectral mixing^{69,70} or tailored higher harmonic excitation⁷¹. Three-color imaging could be readily achieved by combining the different excitation wavelengths and emission filters as we did here. In addition, second-harmonic generation, for example by collagen fibers could be used as a third imaging channel. Collagen is a well-documented second harmonic generating structure which is efficiently excited with IR light, while its emission at 400 nm does not interfere with fluorescent fluorophores used here⁷². By choosing any of abovementioned techniques multi-color imaging can be readily achieved with TPMM allowing for rapid co-localization of structures.

In wide-field imaging of large tissue containing opaque structures, image quality is degraded by scattering of emission photons. Recent TPMM designs address this spatial crosstalk by rejecting scattered photons or redirecting them to correct pixels. Most of these methods however, involve advanced changes to microscope design such as de-scanned detection^{13,52}, wide-spaced multi-anode photomultiplier tubes⁷³ or spinning-disc scanning⁷⁴. For a wider use, background and scattered photons should be suppressed with minimal changes to the design of the microscope. For example, by source-localization of detected photons; Richardson-Lucy deconvolution, relocates scattered photons to their estimated correct pixel without additional optical component⁷⁵. Structured illumination microscopy (SIM) also rejects scattered photons by reconstructing the frequency-modulated illumination pattern. SIM combined with TPMM was shown to increase SNR, imaging depth as well as resolution without changes to the setup^{76,77}, and may further improve image quality by changing from a spiral- to a linear illumination pattern.

In conclusion, we have shown that TPMM yields: fast, high-resolution, low background and stable *in vivo* imaging. It encompasses a favorable balance between bleaching and signal intensity, such that biological processes in cell tissue can be imaged for extended periods of

time and with high temporal resolution. These merits will be especially useful for studying rapid movements of nano-scale objects in long time-lapse studies.

3.5 SUPPLEMENTARY FIGURES

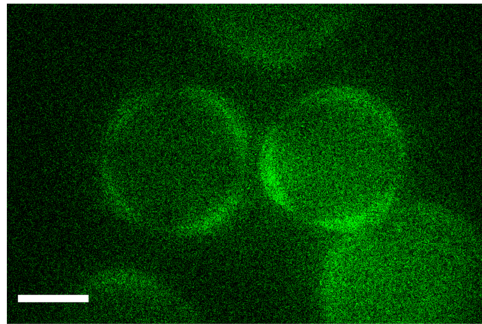


Figure S3.1: TPMM images of two-day old WT pollen grains. No localized signal was detected inside the embryos in absence of the GFP:LEC1 fusion protein. Pollen walls are visible via autofluorescence. Scale bar = 25 μm .

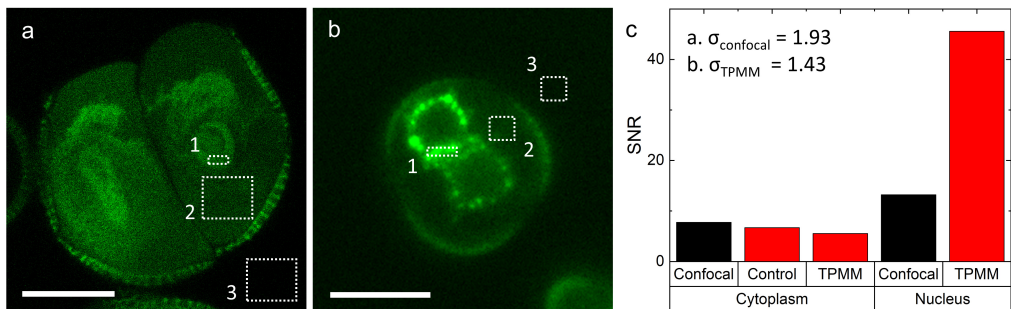


Figure S3.2: By averaging 20 TPMM images, noise (σ) is similar for confocal and TPMM. (a) Confocal image of a three-day old pollen embryo. White squares annotate the region of the nucleus (1), cytoplasm (2) and background (3). Scale bar = 10 μm . (b) Two-photon image of a three-day old pollen, annotated similarly to *a*. Scale bar = 25 μm . (c) SNRs calculated according to equation 3.3 from the mean values of the ROIs as annotated in *a* and *b*. SNR of the cytoplasm of the control measurement was calculated from the image in Figure S1.

3.6 BIBLIOGRAPHY

1. Manzo, C. & Garcia-parajo, M. F. A review of progress in single particle tracking : from methods to biophysical insights. (2015). doi:10.1088/0034-4885/78/12/124601
2. Piyaraj, P. The Green Fluorescent Protein (GFP). *Bangkok Med. J.* **05**, 101–102 (2013).
3. Resch-Genger, U., Grabolle, M., Cavaliere-Jaricot, S., Nitschke, R. & Nann, T. Quantum dots versus organic dyes as fluorescent labels. *Nat. Methods* **5**, 763–775 (2008).
4. Van den Broek, B., Oosterkamp, T. H. & van Noort, J. A Multifocal Two-Photon Microscopy Setup for Parallel 3D Tracking of Gold Nanorods. *Biophys. J.* **98**, 178a (2010).
5. Kilin, V. N. *et al.* Counterion-enhanced cyanine dye loading into lipid nano-droplets for single-particle tracking in zebrafish. *Biomaterials* **35**, 4950–4957 (2014).
6. Li, J. *et al.* Simple and Rapid Functionalization of Gold Nanorods with Oligonucleotides Using an mPEG-SH/Tween 20-Assisted Approach. *Langmuir* **31**, 7869–7876 (2015).
7. So, P. T. C., Dong, C. Y., Masters, B. R. & Berland, K. M. Two-Photon Excitation Fluorescence Microscopy. *Annu. Rev. Biomed. Eng.* 399–429 (2000).
8. Zipfel, W. R., Williams, R. M. & Webb, W. W. Nonlinear magic: Multiphoton microscopy in the biosciences. *Nat. Biotechnol.* **21**, 1369–1377 (2003).
9. Biermann, B. *et al.* Imaging of molecular surface dynamics in brain slices using single-particle tracking. *Nat. Commun.* (2014). doi:10.1038/ncomms4024
10. Diaspro, A., Chirico, G. & Collini, M. Two-photon fluorescence excitation and related techniques in biological microscopy. *Q. Rev. Biophys.* **38**, 97–166 (2005).
11. Drobizhev, M., Makarov, N. S., Tillo, S. E., Hughes, T. E. & Rebane, A. Two-photon absorption properties of fluorescent proteins. *Nat. Methods* **8**, 393–399 (2011).
12. Fittinghoff, D. N., Wiseman, P. W. & Squier, J. A. Widefield multiphoton and temporally decorrelated multifocal multiphoton microscopy. *Opt. Express* **7**, 273 (2000).
13. Martini, J., Andresen, V. & Anselmetti, D. Scattering suppression and confocal detection in multifocal multiphoton microscopy. *J. Biomed. Opt.* **12**, 034010 (2007).
14. Nielsen, T., Fricke, M., Hellweg, D. & Andresen, P. High efficiency beam splitter for multifocal multiphoton microscopy. *J. Microsc.* **201**, 368–376 (2001).
15. Sacconi, L. *et al.* Multiphoton multifocal microscopy exploiting a diffractive optical element. *Opt. Lett.* **28**, 1918 (2003).
16. Poland, S. P. *et al.* Time-resolved multifocal multiphoton microscope for high speed FRET imaging in vivo. *Opt. Lett.* **39**, 6013 (2014).
17. Matsumoto, N. *et al.* Correction of spherical aberration in multi-focal multiphoton microscopy with spatial light modulator. *Opt. Express* **25**, 7055 (2017).
18. Matsumoto, N. *et al.* An adaptive approach for uniform scanning in multifocal multiphoton microscopy with a spatial light modulator. *Opt. Express* **22**, 633 (2014).
19. Nikolenko, V. *et al.* SLM Microscopy: Scanless Two-Photon Imaging and Photostimulation with Spatial Light Modulators. *Front. Neural Circuits* **2**, 5 (2008).
20. Pozzi, P. *et al.* High-throughput spatial light modulation two-photon microscopy for fast functional imaging. *Neurophotonics* **2**, 015005 (2015).
21. Nikolenko, V., Poskanzer, K. E. & Yuste, R. Two-photon photostimulation and imaging

- of neural circuits. *Nat. Methods* **4**, 943–950 (2007).
22. Salomé, R. *et al.* Ultrafast random-access scanning in two-photon microscopy using acousto-optic deflectors. *J. Neurosci. Methods* **154**, 161–174 (2006).
 23. Yang, W. *et al.* Simultaneous Multi-plane Imaging of Neural Circuits. *Neuron* **89**, 269 (2016).
 24. Kazemipour, A. *et al.* Kilohertz frame-rate two-photon tomography. *Nat. Methods* **16**, (2019).
 25. Perillo, E. P. *et al.* Deep and high-resolution three-dimensional tracking of single particles using nonlinear and multiplexed illumination. *Nat. Commun.* **6**, (2015).
 26. Patterson, G. H. & Piston, D. W. Photobleaching in Two-Photon Excitation Microscopy. *Biophys. J.* **78**, 2159–2162 (2000).
 27. Chen, T.-S., Zeng, S.-Q., Luo, Q.-M., Zhang, Z.-H. & Zhou, W. High-Order Photobleaching of Green Fluorescent Protein inside Live Cells in Two-Photon Excitation Microscopy. *Biochem. Biophys. Res. Commun.* **291**, 1272–1275 (2002).
 28. Neutsch, K., Gö-ring, L. & Gerhardt, N. C. Common-path digital holographic microscopy for 3D nanoparticle localization. **1072616**, 41 (2018).
 29. Thompson, R. E., Larson, D. R. & Webb, W. W. Precise nanometer localization analysis for individual fluorescent probes. *Biophys. J.* **82**, 2775–2783 (2002).
 30. Carozza, S., Culkin, J. & Noort, J. Van. Accuracy of the detection of binding events using 3D single particle tracking. *BMC Biophys.* 1–13 (2017). doi:10.1186/s13628-017-0035-8
 31. Proulx, K., Lu, A. & Sumanas, S. Cranial vasculature in zebrafish forms by angioblast cluster-derived angiogenesis. *Dev. Biol.* **348**, 34–46 (2010).
 32. Jin, S. W., Beis, D., Mitchell, T., Chen, J. N. & Stainier, D. Y. R. Cellular and molecular analyses of vascular tube and lumen formation in zebrafish. *Development* (2005). doi:10.1242/dev.02087
 33. Bussmann, J. & Schulte-Merker, S. Unpublished. (2011).
 34. Soriano, M. *et al.* Plasticity in cell division patterns and auxin transport dependency during in vitro embryogenesis in *Brassica napus*. *Plant Cell* **26**, 2568–2581 (2014).
 35. Li, H. *et al.* The histone deacetylase inhibitor trichostatin a promotes totipotency in the male gametophyte. *Plant Cell* **26**, 195–209 (2014).
 36. Custers, J. B. M. Microspore culture in rapeseed (*Brassica napus* L.). in *Doubled Haploid Production in Crop Plants* (Springer, 2003).
 37. Taylor, A. B., Siddiquee, A. M. & Chon, J. W. M. Below melting point photothermal reshaping of single gold nanorods driven by surface diffusion. *ACS Nano* **8**, 12071–12079 (2014).
 38. Lotan, T. *et al.* Arabidopsis LEAFY COTYLEDON1 is sufficient to induce embryo development in vegetative cells. *Cell* **93**, 1195–1205 (1998).
 39. Boulard, C. *et al.* LEC1 (NF-YB9) directly interacts with LEC2 to control gene expression in seed. *Biochim. Biophys. Acta - Gene Regul. Mech.* **1861**, 443–450 (2018).
 40. Morris, J. L. *et al.* Live imaging of collagen deposition during skin development and repair in a collagen I – GFP fusion transgenic zebrafish line. *Dev. Biol.* **441**, 4–11 (2018).
 41. Muntean, B. S. *et al.* A comparative study of embedded and anesthetized zebrafish in vivo on myocardial calcium oscillation and heart muscle contraction. *Front. Pharmacol.* **DEC**, 1–9 (2010).

42. Graham, D. J. L., Tseng, S., Chen, J. H. D. J. & Alexandrakis, G. Dependence of Two-Photon eGFP Bleaching on Femtosecond Pulse Spectral Amplitude and Phase. *J. Fluoresc.* 1775–1785 (2015). doi:10.1007/s10895-015-1667-1
43. Cranfill, P. J. *et al.* Quantitative assessment of fluorescent proteins. *Nat. Methods* **13**, 557–562 (2016).
44. Dittrich, P. S. & Schwille, P. Photobleaching and stabilization of fluorophores used for single-molecule analysis with one- and two-photon excitation. *Appl. Phys. B Lasers Opt.* **73**, 829–837 (2001).
45. Shaner, N. C. *et al.* Improving the photostability of bright monomeric orange and red fluorescent proteins. **5**, 545–551 (2008).
46. Drobizhev, M., Makarov, N. S., Hughes, T. & Rebane, A. Resonance enhancement of two-photon absorption in fluorescent proteins. *J. Phys. Chem. B* **111**, 14051–14054 (2007).
47. Eggeling, C., Widengren, J., Rigler, R. & Seidel, C. A. M. Photobleaching of Fluorescent Dyes under Conditions Used for Single-Molecule Detection: Evidence of Two-Step Photolysis. *Anal. Chem.* **70**, 2651–2659 (1998).
48. Truong, T. V., Supatto, W., Koos, D. S., Choi, J. M. & Fraser, S. E. Deep and fast live imaging with two-photon scanned light-sheet microscopy. *Nat. Methods* **2011 89 8**, 757 (2011).
49. Ji, N., Magee, J. C. & Betzig, E. High-speed, low-photodamage nonlinear imaging using passive pulse splitters. *Nat. Methods* **5**, 197–202 (2008).
50. Corral-Martínez, P. *et al.* Live Imaging of embryogenic structures in Brassica napus microspore embryo cultures highlights the developmental plasticity of induced totipotent cells. *Plant Reprod.* (2020). doi:10.1007/s00497-020-00391-z
51. Niesner, R., Andresen, V., Neumann, J., Spiecker, H. & Gunzer, M. The power of single and multibeam two-photon microscopy for high-resolution and high-speed deep tissue and intravital imaging. *Biophys. J.* **93**, 2519–2529 (2007).
52. Poland, S. P. *et al.* Multifocal multiphoton volumetric imaging approach for high-speed time-resolved Förster resonance energy transfer imaging in vivo. *Opt. Lett.* **43**, 6057 (2018).
53. Kim, K. H. *et al.* Multifocal multiphoton microscopy based on multianode photomultiplier tubes. *Opt. Express* **15**, 11658 (2007).
54. Wang, H. *et al.* In vitro and in vivo two-photon luminescence imaging of single gold nanorods. *Proc. Natl. Acad. Sci. U. S. A.* **102**, 15752–15756 (2005).
55. Sridhar, S. *et al.* In vitro imaging of embryonic stem cells using multiphoton luminescence of gold nanoparticles. *Int. J. Nanomedicine* **2**, 813–819 (2007).
56. Abdelrasoul, G. N. *et al.* PEGylated gold nanorods as optical trackers for biomedical applications: an *in vivo* and *in vitro* comparative study. *Nanotechnology* **27**, 255101 (2016).
57. Durr, N. J. *et al.* Two-photon luminescence imaging of cancer cells using molecularly targeted gold nanorods. *Nano Lett.* **7**, 941–945 (2007).
58. Li, J. L. & Gu, M. Surface plasmonic gold nanorods for enhanced two-photon microscopic imaging and apoptosis induction of cancer cells. *Biomaterials* **31**, 9492–9498 (2010).
59. Gonzalez-Moragas, L. *et al.* In vivo testing of gold nanoparticles using the Caenorhabditis elegans model organism. *Acta Biomater.* (2017).

- doi:10.1016/j.actbio.2017.01.080
60. Li, D. *et al.* Graphene oxide nanoparticles for two-photon fluorescence imaging of zebrafish. *Opt. Quantum Electron.* **48**, (2016).
 61. Ali, M. R. K., Ali, H. R., Rankin, C. R. & El-Sayed, M. A. Targeting heat shock protein 70 using gold nanorods enhances cancer cell apoptosis in low dose plasmonic photothermal therapy. *Biomaterials* **102**, 1–8 (2016).
 62. Riley, R. S. & Day, E. S. Gold nanoparticle-mediated photothermal therapy: applications and opportunities for multimodal cancer treatment. *Wiley Interdiscip. Rev. Nanomedicine Nanobiotechnology* **9**, e1449 (2017).
 63. Molotkovsky, J. G. Fluorescent lipid probes: Properties and application. *Russ. J. Bioorganic Chem.* **25**, 759–771 (1999).
 64. Campbell, F. *et al.* Directing Nanoparticle Biodistribution through Evasion and Exploitation of Stab2-Dependent Nanoparticle Uptake. *ACS Nano* **12**, 2138–2150 (2018).
 65. Li, H. *Microspore embryogenesis: Reprogramming Cell Fate from Pollen to Embryo Development.* (2014).
 66. Cheung, A. Y., Boavida, L. C., Aggarwal, M., Wu, H. M. & Feijó, J. A. The pollen tube journey in the pistil and imaging the in vivo process by two-photon microscopy. *J. Exp. Bot.* **61**, 1907–1915 (2010).
 67. Gooh, K. *et al.* Live-Cell Imaging and Optical Manipulation of Arabidopsis Early Embryogenesis. *Dev. Cell* **34**, 242–251 (2015).
 68. Ohtsu, M. *et al.* Fluorescent Labeling of the Cyst Nematode *Heterodera glycines* in Deep-Tissue Live Imaging. *Cytologia (Tokyo)*. **82**, 251–259 (2017).
 69. Mizuta, Y., Kurihara, D. & Higashiyama, T. Two-photon imaging with longer wavelength excitation in intact Arabidopsis tissues. *Protoplasma* **252**, 1231–1240 (2015).
 70. Mahou, P. *et al.* Multicolor two-photon tissue imaging by wavelength mixing. *Nat. Methods* **9**, 815–818 (2012).
 71. Stringari, C. *et al.* Multicolor two-photon imaging of endogenous fluorophores in living tissues by wavelength mixing. *Sci. Rep.* **7**, 1–11 (2017).
 72. Tillo, S. E., Hughes, T. E., Makarov, N. S., Rebane, A. & Drobizhev, M. A new approach to dual-color two-photon microscopy with fluorescent proteins. *BMC Biotechnol.* **10**, 2–7 (2010).
 73. Zoumi, A., Yeh, A. & Tromberg, B. J. Imaging cells and extracellular matrix in vivo by using second-harmonic generation and two-photon excited fluorescence. *Proc. Natl. Acad. Sci. U. S. A.* **99**, 11014–11019 (2002).
 74. Cha, J. W. *et al.* Non-descanned multifocal multiphoton microscopy with a multianode photomultiplier tube. *AIP Adv.* **5**, 084802 (2015).
 75. Rakotoson, I. *et al.* Fast 3-D Imaging of Brain Organoids With a New Single-Objective Planar-Illumination Two-Photon Microscope. *Front. Neuroanat.* **13**, 1–14 (2019).
 76. Quicke, P. *et al.* High speed functional imaging with source localized multifocal two-photon microscopy. *Biomed. Opt. Express* **9**, 3678 (2018).
 77. Hagen, G. M., Fliegel, K., Republic, C. & Republic, C. Comparison of image reconstruction methods for structured illumination microscopy. **9129**, 1–13 (2014).
 78. Ingaramo, M. *et al.* Two-photon excitation improves multifocal structured illumination microscopy in thick scattering tissue. *Proc. Natl. Acad. Sci.* **111**, 5254–5259 (2014).